

# Feature Extraction and Classification Based on Spatial-Spectral ConvLSTM Neural Network for Hyperspectral Images

Wen-Shuai Hu, Heng-Chao Li, *Senior Member, IEEE*, Lei Pan, Wei Li, *Senior Member, IEEE*, Ran Tao, *Senior Member, IEEE*, and Qian Du, *Fellow, IEEE*

**Abstract**—In recent years, deep learning has presented a great advance in hyperspectral image (HSI) classification. Particularly, Long Short-Term Memory (LSTM), as a special deep learning structure, has shown great ability in modeling long-term dependencies in the time dimension of video or the spectral dimension of HSIs. However, the loss of spatial information makes it quite difficult to obtain the better performance. In order to address this problem, two novel deep models are proposed to extract more discriminative spatial-spectral features by exploiting the Convolutional LSTM (ConvLSTM) for the first time. By taking the data patch in a local sliding window as the input of each memory cell band by band, the 2-D extended architecture of LSTM is considered for building the spatial-spectral ConvLSTM 2-D Neural Network (SSCL2DNN) to model long-range dependencies in the spectral domain. To take advantage of spatial and spectral information more effectively for extracting a more discriminative spatial-spectral feature representation, the spatial-spectral ConvLSTM 3-D Neural Network (SSCL3DNN) is further proposed by extending LSTM to 3-D version. The experiments, conducted on three commonly used HSI data sets, demonstrate that the proposed deep models have certain competitive advantages and can provide better classification performance than other state-of-the-art approaches.

**Index Terms**—Hyperspectral image, Convolutional Long Short-Term Memory, deep learning, feature extraction, classification.

## I. INTRODUCTION

THE hyperspectral remote sensing image is a 3-D data cube, which integrates the spectral information with the 2-D spatial information of land covers. With the development of remote sensing technology, together with the continuous improvement of hyperspectral sensors,

This work was supported in part by the National Natural Science Foundation of China under Grant 61871335, and by the Frontier Intersection Basic Research Project for the Central Universities under Grant A0920502051814-5.

W.-S. Hu, H.-C. Li, and L. Pan are with the Sichuan Provincial Key Laboratory of Information Coding and Transmission, Southwest Jiaotong University, Chengdu 610031 China.

W. Li and R. Tao are with the School of Information and Electronics, Beijing Institute of Technology, Beijing 100081 China.

Q. Du is with the Department of Electrical and Computer Engineering, Mississippi State University, Mississippi State, MS 39762 USA.

hyperspectral image (HSI) can provide more opportunities to manage and analyze the information from the Earth’s surface [1]-[3]. Correspondingly, HSIs have been widely used in many fields, such as environmental sciences [2], precision agriculture [4], [5], ecological science [6], and geological exploration [7].

As a basic and important research topic, HSI classification has attracted plenty of attentions. The support vector machine (SVM) is the most widely used classifier and shows great success in HSI classification [8], [9]. Especially, a composite kernel SVM (SVM-CK) was proposed to exploit the spatial and spectral information simultaneously [10]. Inspired by the successful application on face recognition [11], sparse representation (SR) [12] has also been applied in HSI classification, which was further improved to exploit the spatial information by Chen *et al.* in [13], resulting in a joint SR classifier (JSRC). Subsequently, more and more classifiers based on joint sparse model were developed, such as non-local weighted JSRC (NLW-JSRC) [14], nearest regularized JSRC (NRJSRC) [15], and correntropy-based robust JSRC (RJSRC) [16].

In recent years, deep learning has presented a great advance for feature extraction and classification in the field of computer vision, such as object detection [17], object tracking [18], and behavior recognition in crowd scene [19], and also shown the effectiveness in HSI classification tasks [20]. An increasing number of feature extraction and classification methods based on deep learning framework have been designed for HSIs, such as Deep Belief Network (DBN) [21], Convolutional Neural Network (CNN) [22], presenting great improvement on the performance. In [23], a classification method based on Stacked AutoEncoder (SAE) was exploited for HSI classification for the first time by extracting spatial-spectral features. Since Hu *et al.* [22] and Chen *et al.* [24] introduced CNN into HSI classification, many new classification models based on CNN have emerged and provided satisfying performance in HSI classification. Inspired by SVM-CK [10] and CNN [22], Mei *et al.* [25] proposed a new model based on CNN by using the mean of local patch of central pixel at each band. Li *et al.*

[26] integrated the pixel-pair method and CNN to further obtain discriminative features. Zhao and Du [27] utilized CNN and the balanced local discriminant embedding to fuse spatial and spectral information. For the sake of joint learning of spatial and spectral features, many classification structures [28]-[30] were also built for taking the 3-D data cube as the input of neural network. In addition, to overcome the problem of the limitation of available labeled samples, two self-taught learning frameworks based on the multiscale Independent Component Analysis (MICA) and the Stacked Convolutional Autoencoder (SCAE) [31], semisupervised CNN [32], and a supervised deep feature extraction method based on Siamese CNN (S-CNN) [33] were proposed. In addition to the single-channel deep network models, there are also some novel work [30], [34] based on multi-channel CNN to improve feature extraction and classification.

Obviously, CNN has provided an extremely effective and basic structure for various tasks, and become the core architecture of various models, such as VGG16 [17], ResNet [36], CapsNets [37], DenseNet [38], among which the convolutional layer is the core backbone for feature extraction. In order to address the gradient vanishing problem caused by deeper and deeper network structures [35], effective feature extraction and classification models [36]-[38] were proposed to improve the classification performance for HSIs by promoting the CNN filters.

For general-purpose sequence modeling, Long Short-Term Memory (LSTM), as an exception Recurrent Neural Network (RNN) structure [39], has demonstrated its stability and power in modeling long-term dependencies in various studies [40]-[42]. The initially proposed structure of LSTM utilizes the special “memory cells” instead of logistic or tanh hidden units [40], and there are three significant gate mechanisms in this kind of structure: input gate, output gate, and forget gate, which are used for implementing information protection, transmission, and control, respectively. Specifically, the input gate is applied to control when the input is allowed to be added to the memory cell, the output gate is designed to decide when the input data has an influence on the output of the memory cell, and forget gate, as the key structure in LSTM, is mainly used for modeling long-range dependencies. It is the design of this special memory cell with fixed weight and self-connected circular edges that ensures the gradient can pass across many time steps without gradient vanishing or explosion problems [43].

In the interest of effectively analyzing sequential data, RNN [39], LSTM [44], [45], and 3-D CNN [46] have been constructed to cope with this kind of task. Especially, due to the special internal structure of RNN (or LSTM), more attentions have been paid to this structure. Based on CNN and RNN (or CNN and LSTM) framework, some novel deep structures have been applied to a

great number of research tasks, such as facial expression recognition [47], script identification [48], and video captioning [49], which is the most common way to combine LSTM with CNN, and can yield satisfying performance.

Since Zhou *et al.* [50] first designed a spatial-spectral LSTMs (SSLSTMs) based on two independent LSTMs in the way of spatial LSTM (SaLSTM) and spectral LSTM (SeLSTM), it has been proved that LSTM can be used to model long-term dependencies in spatial domain or spectral domain for HSI feature extraction and classification. However, there is a major drawback in LSTM when handling spatial-spectral or spatial-temporal data, that is, the special structure of LSTM makes it necessary to unfold the input data to the 1-D data. Unfortunately, the intrinsic spatial information of the input data may be lost after this transformation. In order to better model spatial-temporal relationships well, Shi *et al.* [51] extended the 1-D data processing of each gate unit in LSTM to multi-dimensional operation realized by convolution and proposed Convolutional LSTM (ConvLSTM) that was made up of convolution structures in both the input-to-state and state-to-state transitions. Depending on the convolution structures in ConvLSTM, ConvLSTM2D with a 2-D convolution filter and ConvLSTM3D with a 3-D convolution filter can be constructed. Inspired by this, a model based on Bidirectional-Convolutional LSTM [52] was proposed to extract the spatial-spectral feature for HSI classification.

Although ConvLSTM is also composed of convolution structures similar to the operation in CNN, its special internal structure design in each memory cell makes it possible to capture more valuable information from the input data, and produce more discriminative feature representations. On the other hand, in all applications of LSTM and its variant, they are used either in combination with CNN [47]-[49] or in isolation [50].

Inspired by the above work, the main purpose of this paper is to construct a novel deep neural network structure based on ConvLSTM for HSI feature extraction and classification. First of all, the spatial-spectral ConvLSTM 2-D Neural Network (SSCL2DNN) is proposed to construct a joint spatial-spectral deep model based on ConvLSTM2D. Specially, when changing the time\_step and the input data in SSCL2DNN, it will degenerate into the spatial ConvLSTM 2-D Neural Network (SaCL2DNN). Moreover, based on the single-band independent convolution operation in each memory cell of ConvLSTM2D, it is expected to obtain relatively good classification performance. However, the way of extracting spatial-spectral features by modeling long-range dependencies in spectral domain may not be the most effective approach, which means the intrinsic structure of the hyperspectral data may be destroyed when taking each band component of the data cube as the input

of each corresponding memory cell. In other words, the correlations and dependencies between different spectral bands may not be effectively utilized.

As such, the 3-D extended architecture of LSTM (ConvLSTM3D) is further considered in this paper. With the help of ConvLSTM3D, the spatial-spectral ConvLSTM 3-D Neural Network (SSCL3DNN) is proposed to further improve the classification performance. The main contributions of this paper are listed as follows:

- (1) It is the first time that ConvLSTM2D is used as a fundamental network to construct novel deep models for HSI feature extraction and classification. Specifically, a spatial-spectral deep feature extraction network, i.e., SSCL2DNN, is first proposed. As a byproduct, another deep model, i.e., SaCL2DNN, can be obtained by using different parameters and data form of ConvLSTM2D.
- (2) In order to explore the intrinsic spatial structure of hyperspectral data, on the basis of ConvLSTM2D, the 3-D extended architecture (ConvLSTM3D) is further developed, and finally a novel and effective deep model, i.e., SSCL3DNN, is constructed, which can perform better than SSCL2DNN.
- (3) To demonstrate the effectiveness of our proposed deep models, three real HSI data sets are adopted. The experimental results from perspectives of classification accuracy and classification map show the superiority when compared with other state-of-the-art methods. and computational complexity

The remainder of this paper is organized as follows. Section II presents CNN and LSTM, and discusses the applications on HSI feature extraction and classification. In Sections III and IV, the proposed deep models with the extraction of spatial-spectral features for HSI classification are described in detail, respectively. Comprehensive quantitative analysis and evaluation of the proposed models are implemented in Section V. And conclusively, Section VI summarizes this paper.

## II. RELATED WORK

In this section, we first provide an overview of CNN that has a close connection with the deep models constructed in this paper. Then, a brief introduction for LSTM and its extended version is given, which also is the core backbone of our proposed deep models.

### A. Convolutional Neural Network

The fundamental CNN mainly consists of the following parts: convolutional layer, pooling layer, full connection layer, and classification layer. The common structure of CNN is shown in Fig. 1. Based on different convolution operations, we can construct various networks to meet a variety of practical requirements.

Originally, the calculation formula of each convolutional layer in CNN can be expressed as

$$o_{l+1} = \phi(W_l * o_l + b_l), \quad (1)$$

where  $o_{l+1}$  is the output with  $n$  feature maps of the  $l$ th convolutional layer,  $W_l$  denotes the convolution filter, and  $b_l$  is the bias of the  $l$ th convolutional layer,  $o_l$  is the output of the  $(l-1)$ th convolutional layer, and  $\phi(\cdot)$  is the nonlinear activation function.  $W_l$  has a size of  $k^{(l)} \times k^{(l)}$  for 2-D CNN. With respect to 3-D CNN,  $W_l$  is a convolution filter in the  $l$ th convolutional layer with the size of  $k^{(l)} \times k^{(l)} \times d^{(l)}$ , in which  $k^{(l)}$  and  $d^{(l)}$  denote the size and depth of the convolution filter, respectively.

Since Hu *et al.* [22] and Chen *et al.* [24] proposed HSI feature extraction and classification models based on CNN, more and more improved CNN-based models have been introduced. CNN has become an extremely effective and basic structure for various tasks. It is noteworthy that a sliding window is still used to extract spatial features in CNN, which is a traditional way of exploiting spatial information. Moreover, the data transmission and processing in CNN only exist one layer and another, lacking information interaction inside each layer, which may make it quite difficult to extract a more effective feature representation.

### B. Long Short-Term Memory

LSTM is proposed to deal with the issues that RNN is not suitable for learning long-term dependencies and prone to bring about gradient vanishing and exploding problems [43]. The network structure of LSTM can be found in Fig. 2. It is obvious that the data transmission and processing in LSTM are realized by three key gate units: input gate, output gate, and forget gate, which are used for implementing information protection and control [40]. The calculation formulas between these three gate structures in LSTM are written as

$$\begin{aligned} i_t &= \sigma(W_{xi}x_t + W_{hi}h_{t-1} + W_{ci}c_{t-1} + b_i) \\ f_t &= \sigma(W_{xf}x_t + W_{hf}h_{t-1} + W_{cf}c_{t-1} + b_f) \\ \tilde{c}_t &= \tanh(W_{xc}x_t + W_{hc}h_{t-1} + b_c) \\ c_t &= f_t \circ c_{t-1} + i_t \circ \tilde{c}_t \\ o_t &= \sigma(W_{xo}x_t + W_{ho}h_{t-1} + W_{co} \circ c_t + b_o) \\ h_t &= o_t \circ \tanh(c_t), \end{aligned} \quad (2)$$

where  $x_t$ ,  $h_{t-1}$ , and  $c_{t-1}$  represent the input of the current cell, the output and state of the last cell in LSTM, respectively.  $i_t$ ,  $f_t$ , and  $h_t$  denote the input gate, output gate, and forget gate of LSTM.  $W_{\bullet i}$  and  $b_i$  are the weight and bias of the input gate,  $W_{\bullet f}$  and  $b_f$  are the weight and bias of the forget gate, and  $W_{\bullet o}$  and  $b_o$  are the weight and bias of the output gate, where  $\bullet$  indicates  $x$ ,  $h$ , and

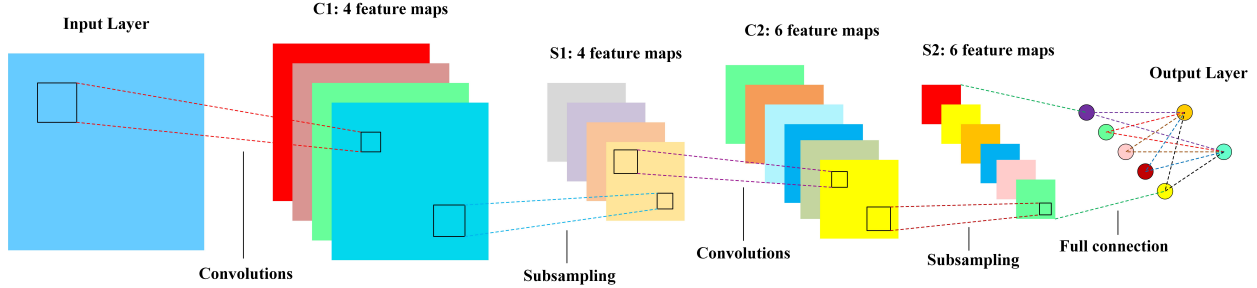


Fig. 1. The common network structure of CNN.

$c \circ$  denotes the Hadamard product.  $\sigma$  is the nonlinear activation function.

Inspired by this, Zhou *et al.* [50] first attempted to apply LSTM to HSI classification and advanced the spatial-spectral LSTMs (SSLSTMs). The experimental results show that LSTM can also be well used for modeling long-range dependencies in spectral domain. Nevertheless, it is worth noting that the two branches in SSLSTMs are independent of each other. In addition, the unfolding of the original HSI data to one-dimensional vectors as the input of SSLSTMs will actually lose the intrinsic structure of the hyperspectral data, since spatial information is not considered in LSTM.

### C. Convolutional LSTM

Considering the shortcomings of LSTM, a modification and extended version of LSTM, i.e., ConvLSTM [51], is developed. Different with LSTM, the input-to-state and state-to-state transitions in ConvLSTM are implemented by convolution structures. Based on different convolution structures, ConvLSTM2D and ConvLSTM3D can be obtained. Specially, these two extensions hold the same network structure with LSTM and can also be applied to model long-term dependencies in the time domain or spectral domain. The illustration of the inner structure of ConvLSTM is shown in Fig. 3, in which the calculation formulas can be expressed as

$$\begin{aligned}
 i_t &= \sigma(W_{xi} * X_t + W_{hi} * H_{t-1} + W_{ci} \circ C_{t-1} + b_i) \\
 f_t &= \sigma(W_{xf} * X_t + W_{hf} * H_{t-1} + W_{cf} \circ C_{t-1} + b_f) \\
 \tilde{C}_t &= \tanh(W_{xc} * X_t + W_{hc} * H_{t-1} + b_c) \\
 C_t &= f_t \circ C_{t-1} + i_t \circ \tilde{C}_t \\
 o_t &= \sigma(W_{xo} * X_t + W_{ho} * H_{t-1} + W_{co} \circ C_t + b_o) \\
 H_t &= o_t \circ \tanh(C_t),
 \end{aligned} \tag{3}$$

where  $X_t$  denotes the input of the current cell,  $C_{t-1}$  and  $H_{t-1}$  are state and output of the last cell, respectively.  $*$  means the convolution operation.  $W$ , similar to the convolutional layers in CNN, denotes the convolution filter, which may be a 2-D convolution filter with a  $k \times k$  kernel or a 3-D convolution filter with a  $k \times k \times d$  kernel,  $k$  and  $d$  are the size and depth of the convolution kernel,

respectively. Specially, the definitions of  $W_{\bullet i}$ ,  $W_{\bullet f}$ ,  $W_{\bullet o}$ ,  $b_i$ ,  $b_f$ , and  $b_o$  are similar to that in (2), however, the data dimensions and processing methods are different.

Different from the traditional way of extracting spatial features based on sliding window in CNN, ConvLSTM holds three special gate mechanisms to complete data transmission and processing, which makes it possible to utilize spatial information of HSIs more effectively. Simultaneously, ConvLSTM can not only implement data transmission and processing of the inter-layer, but also execute those of the intra-layer, which is another great difference from CNN. This special structure enables ConvLSTM to extract the more effective feature representation than CNN. Furthermore, compared with LSTM, the implementations of three gate mechanisms are extended from one-dimensional to multi-dimensional convolution operation, and this change can not only capture the spatial context information of the original data similar to the convolutional layer in CNN, but also model the long-range dependencies in the time domain of video [47] or the spectral domain of HSIs [50].

## III. SPATIAL-SPECTRAL CONVLSTM 2-D NEURAL NETWORK (SSCL2DNN)

In the previous work, LSTM or its variant was used either in combination with CNN [47]-[49] or in isolation [50]. However, how to effectively combine LSTM with CNN will have a great impact on the final performance, which is a extremely important research topic. In addition, due to the limitation of feature extraction of LSTM [48], much more layers of LSTM or its variant are required to yield good performance. These problems motivated us to build a novel deep neural network based on ConvLSTM for HSI feature extraction and classification. In particular, it should be pointed out that ConvLSTM involved in this section is actually a 2-D extension form of LSTM, i.e., ConvLSTM2D.

### A. SSCL2DNN

On account of the above analysis, a joint spatial-spectral feature extraction and classification model based on ConvLSTM2D is constructed, which is shown in Fig. 4 labeled by ① with blue. The core structure of our

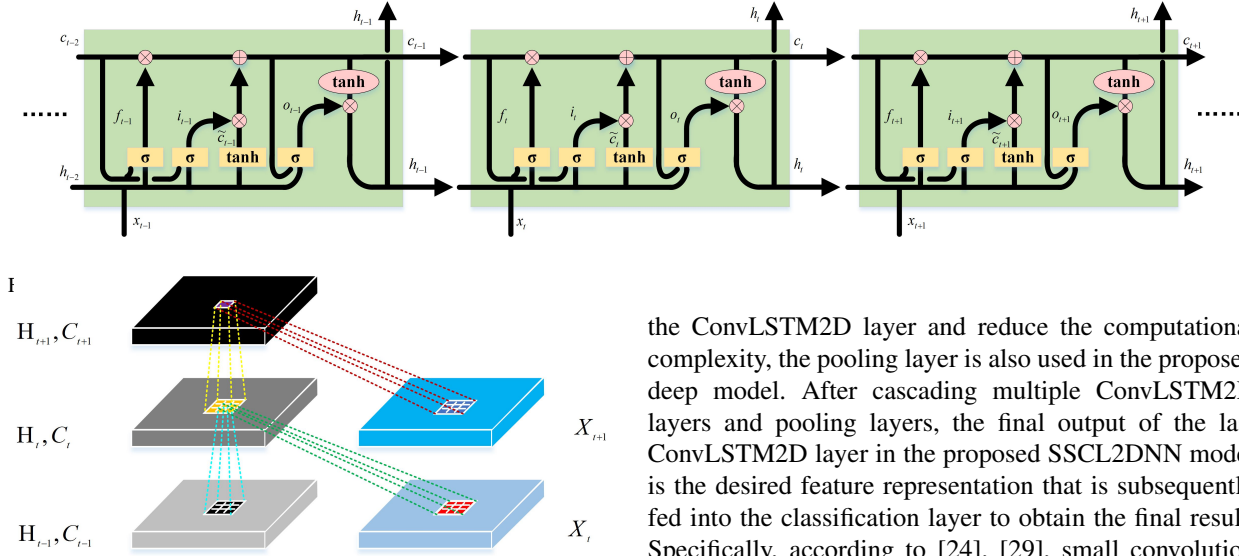


Fig. 3. The illustration of the inner structure of ConvLSTM

proposed SSCL2DNN model consists of ConvLSTM2D layer and pooling layer. Based on the special structure of ConvLSTM2D, a 3-D data containing spectral and spatial information is input in each ConvLSTM2D layer. However, there are many redundant information in original HSI data cubes, and the more data used, the greater complexity involved. Unlike [24], PCA is selected as the preprocessing method to implement dimension reduction of data.

First of all, the size of the original HSI data cube can be denoted as  $W \times H \times D$ , where  $D$  indicates the number of the spectral bands,  $W$  and  $H$  are the width and height of HSI, respectively. Then, the spectral information of HSI is considered, and the first  $K$  principal components in PCA are selected as the spectral information of each pixel  $x_i$ . Furthermore, for each ConvLSTM2D layer in SSCL2DNN, considering that the spatial context information is beneficial to HSI classification, the data in a local spatial window with the size of  $s \times s$  is extracted as the spatial information for extracting spatial-spectral features, which is the input of each memory cell in the ConvLSTM2D layer. After data preprocessing, a 3-D input data denoted by  $s \times s \times K$  is constructed. In particular, suppose that the special dimension  $\text{time\_step}$  in ConvLSTM is expressed as a variable  $\tau$ , and it needs to be fixed as  $K$  in order to correspond to the dimension of the input in each ConvLSTM2D layer. Concretely, the 3-D input of each pixel  $x_i$  is decomposed into  $K$  2-D components and converted into a sequence with the length of  $K$ , i.e.,  $\{X_i^1, \dots, X_i^k, \dots, X_i^K\}$ ,  $k \in \{1, 2, \dots, K\}$ , where  $X_i^k$  denotes the  $k$ th component of the pixel  $x_i$ . Then, this sequence is fed into the ConvLSTM2D layer one by one.

In order to compress the feature maps generated by

the ConvLSTM2D layer and reduce the computational complexity, the pooling layer is also used in the proposed deep model. After cascading multiple ConvLSTM2D layers and pooling layers, the final output of the last ConvLSTM2D layer in the proposed SSCL2DNN model is the desired feature representation that is subsequently fed into the classification layer to obtain the final result. Specifically, according to [24], [29], small convolution kernels are efficient for yielding better classification performance. As such, the size of the convolution kernels in our proposed deep model can be set as  $4 \times 4$  or  $3 \times 3$ , and the kernel size of  $2 \times 2$  is adopted to implement the operation of the pooling layer.

Due to the exceptional inner structure of LSTM and its extended architecture, it is evident that if we set  $\tau$  to 1 and  $K$  to 1 in each ConvLSTM2D layer, and convert the input from a 3-D data to a 2-D data, the proposed deep model is reduced to spatial ConvLSTM 2-D Neural Network (SaCL2DNN), which is shown in Fig. 4 labeled by ② with the red dotted boxes. Specially, similar to 2-D CNN in [24], the first principal component is selected to construct a 2-D input for SaCL2DNN for the reason that it contains the most energy of the original HSI.

Based on the ConvLSTM2D cell, by adjusting different input and parameter  $\text{time\_step}$  of the ConvLSTM2D layer, two new deep neural networks will be constructed for HSI feature extraction and classification, i.e., SaCL2DNN with spatial features and SSCL2DNN with spatial-spectral features.

Particularly, the proposed deep models can not only implement the same data transmission between layers as CNN does, but also accomplish effective data transmission and processing within each ConvLSTM2D layer. It is known that adjacent spectral bands are highly correlated, and there may also be some correlation between non-adjacent spectral bands [53]. Therefore, our proposed SSCL2DNN model can also be used to model long-range dependencies in the spectral field, which may provide more discriminative spatial-spectral feature representations than the 2-D operation. Compared with SSLSTMs in [50], the proposed deep models can obtain more discriminative features by jointly considering the spatial-spectral information of HSIs, which successfully address the problem caused by using two sub-branches independently.

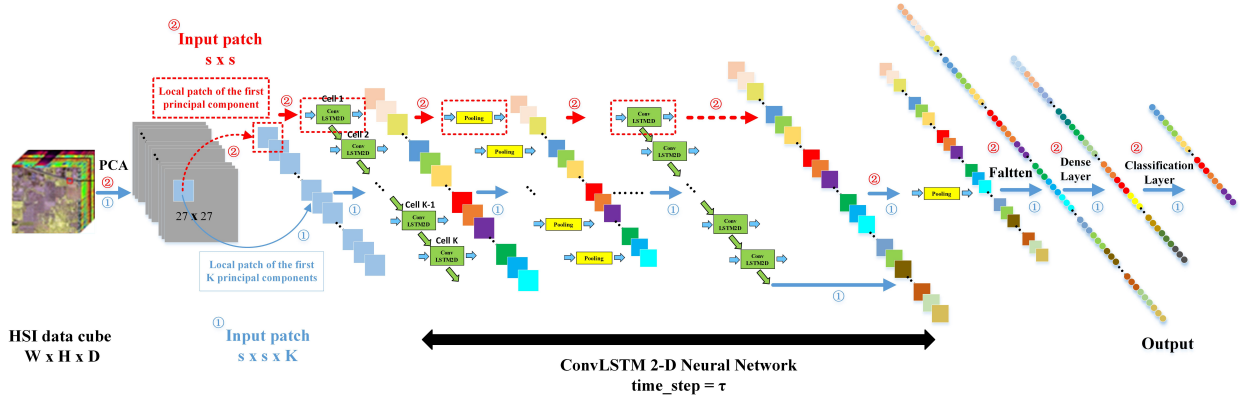


Fig. 4. The proposed spatial-spectral ConvLSTM 2-D Neural Network (SSCL2DNN) is labeled by ① with blue. In particular, SSCL2DNN can be transformed into another deep model when  $K$  equals 1 and  $\tau$  equals 1, which is called spatial ConvLSTM 2-D Neural Network (SaCL2DNN) labeled by ② with red dotted box.

### B. Loss Function and Optimization Method

By stacking multiple ConvLSTM2D layers and pooling layers in SSCL2DNN and SaCL2DNN, more effective features are extracted and fed into the classification layer to predict the conditional probability distribution of each class as

$$P(y = i|x, W, b) = \frac{e^{(W_{ix} + b_i)}}{\sum_{j=1}^N (e^{(W_{jx} + b_j)})}, \quad (4)$$

where  $W$  and  $b$  are the weight and bias of the classification layer, respectively.

In addition, the cross entropy is used as the loss function to obtain the final classification result, which can be described as

$$L_{loss}(Y, \tilde{Y}) = - \sum (Y \cdot \log(\tilde{Y})), \quad (5)$$

where  $Y$  and  $\tilde{Y}$  are the ground truth available in original HSI data sets and the corresponding predictive value of our deep models, respectively.

By using the ADAM algorithm for the optimization of our loss function, the probability value  $P(y = j|x_i), j \in 1, 2, \dots, N$  of each pixel  $x_i$  can be obtained, where  $N$  indicates the number of classes in the HSI data sets.

## IV. SPATIAL-SPECTRAL CONVLSTM 3-D NEURAL NETWORK (SSCL3DNN)

Although SSCL2DNN may yield relatively good classification performance, the way of extracting spatial-spectral features by modeling long-range dependencies in spectral domain may not be the most effective approach, because the intrinsic structure of HSIs may be destroyed when taking each band component of the data patch as the input of each corresponding memory cell. Therefore, it may not be an elaborate spatial-spectral feature extraction method for HSI classification. This motivates us to design a better deep network to capture the intrinsic structure of the hyperspectral data.

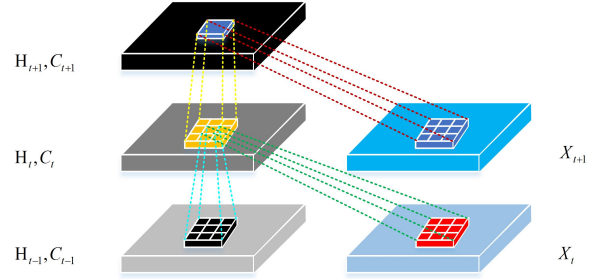


Fig. 5. The illustration of the inner structure of ConvLSTM3D

### A. ConvLSTM3D

The illustration of the inner structure of ConvLSTM3D can be found in Fig. 5. There are also three gate units similar to ConvLSTM2D, and the calculation formulas between these three gate units are similar to that in ConvLSTM2D as shown in (2). However, different from ConvLSTM2D, the 3-D data with a size of  $s \times s \times K$  is taken as the input of each memory cell in ConvLSTM3D. Interestingly, although this difference between ConvLSTM2D and ConvLSTM3D is similar to that between 2-D CNN and 3-D CNN, three special gate units make it possible to extract a more discriminative feature representation for HSI classification.

Moreover, the convolution kernel in ConvLSTM3D cell, similar to that in 3-D CNN, needs to be extended from 2-D convolution filter with a  $k \times k$  kernel in ConvLSTM2D cell to 3-D convolution filter with a  $k \times k \times d$  kernel, where  $k$  and  $d$  are the kernel size and the depth of the convolution filter, respectively.

### B. SSCL3DNN

According to the extraordinary structure of ConvLSTM3D, we further extend SSCL2DNN to a new deep model based on ConvLSTM3D, i.e., SSCL3DNN. Different from SSCL2DNN, the whole data cube must be taken as the input of the memory cell in SSCL3DNN. Therefore, the intrinsic structure of HSIs can be captured

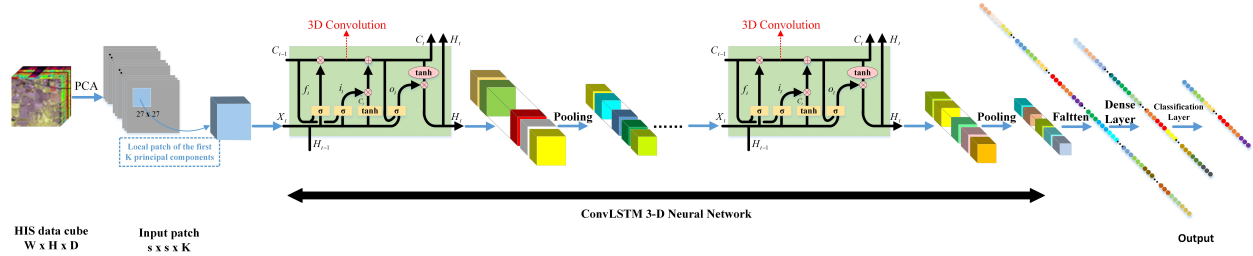


Fig. 6. The proposed spatial-spectral ConvLSTM 3-D Neural Network (SSCL3DNN) structure.

well, and the spatial-spectral features can be well learned to further improve the HSI classification performance. Fig. 6 clearly shows the structure of the proposed deep model, and the parameter  $\tau$  is fixed as 1.

Especially, PCA is also used to reduce the redundant information in this section, and the first  $K$  components are chosen. With regard to the selection of the size of the convolution kernel, the small kernel size is also considered, which can be set as  $3 \times 3 \times 3$  or  $5 \times 5 \times 5$  in the proposed deep model. Besides, the size of the pooling kernel in the pooling layer is set as  $2 \times 2 \times 2$ . After the cascade of multiple ConvLSTM3D layers and pooling layers, the spatial-spectral features are extracted from the 3-D data cube and subsequently fed into the classification layer to obtain the final classification result.

The loss function and optimization method are the same as those of the proposed SSCL2DNN model.

## V. EXPERIMENTAL RESULTS

To quantitatively and qualitatively analyze the classification performance of the proposed deep models, SVM [54], 2-D CNN [24], 3-D CNN [24], SaLSTM [50], and SSLSTMs [50] are used as the comparative algorithms. Three commonly used quantitative metrics are adopted, i.e., overall accuracy (OA), average accuracy (AA), and Kappa coefficient ( $\kappa$ ). To eliminate the bias introduced by randomly choosing training samples, each experiment is repeated ten times, and the mean values of each evaluation criterion are presented.

### A. Hyperspectral Data Sets

Three common HSI data sets, i.e., Indian Pines, Salinas Valley, and University of Pavia, are considered in our experiments, whose false color maps, ground truth maps, and the corresponding training size are shown in Fig. 7, respectively.

1) *Indian Pines*: The Indian Pines data set was captured in 1992 by the Airborne Visible/Infrared Imaging Spectrometer (AVIRIS) sensor in Northwestern Indiana, USA, which is mainly composed of multiple agricultural fields. The spatial size of this data set is  $145 \times 145$  pixels with a spatial resolution of 20 meters per pixel (mpp),

and there are 224 spectral bands in the wavelength range from  $0.4$  to  $2.5 \mu\text{m}$ . Since some of them cannot be reflected by water together with four null bands, there are generally 200 bands remaining for study. After removing the background pixels, 10249 pixels are reserved, which contain useful ground-truth information from 16 different class labels.

2) *Salinas Valley*: The Salinas Valley data set was collected by the 224-band AVIRIS sensor over Salinas Valley, California. This data set is made up of 512 lines and 217 columns, and contains 16 ground-truth classes. After removing the water absorption bands and noise-affected bands, there are 204 spectral bands preserved.

3) *University of Pavia*: The University of Pavia data set was acquired by the Reflective Optics System Imaging Spectrometer (ROSIS) sensor over University of Pavia, Northern Italy. There are 103 spectral bands in the spectral range from  $0.43$  to  $0.86 \mu\text{m}$  by removing several noise-corrupted bands, and it presents a size of  $610 \times 340$  pixels with a spatial resolution of 1.3 mpp. Different from the Indian Pines and Salinas Valley data sets, this data set contains 9 distinguishable classes.

### B. Experimental Settings

Since the first principal component in PCA contains the most valuable information of the original HSI data sets, PCA is selected to preserve only one component for SVM, 2-D CNN, SaLSTM, and the proposed SaCL2DNN model. As for 3-D CNN, SSLSTMs, the proposed SSCL2DNN and SSCL3DNN models, after considering the redundancy and complexity of the original hyperspectral data, PCA is also used to extract the top  $K$  principal components as the preserved spectral features. Specially, for SeLSTM [50], all spectral bands of each pixel in these three data sets are used for constructing 1-D vectors.

All the parameters of the compared methods are confirmed according to [24], [50], [54] to achieve the best performance. Specifically, for SVM, the Gaussian radial basis function (RBF) is used by adopting the Libsvm toolbox [54]. There are two key parameters in SVM, i.e.,  $C$  and  $\gamma$ , which denote the regularization parameter and the kernel function parameter, respectively.

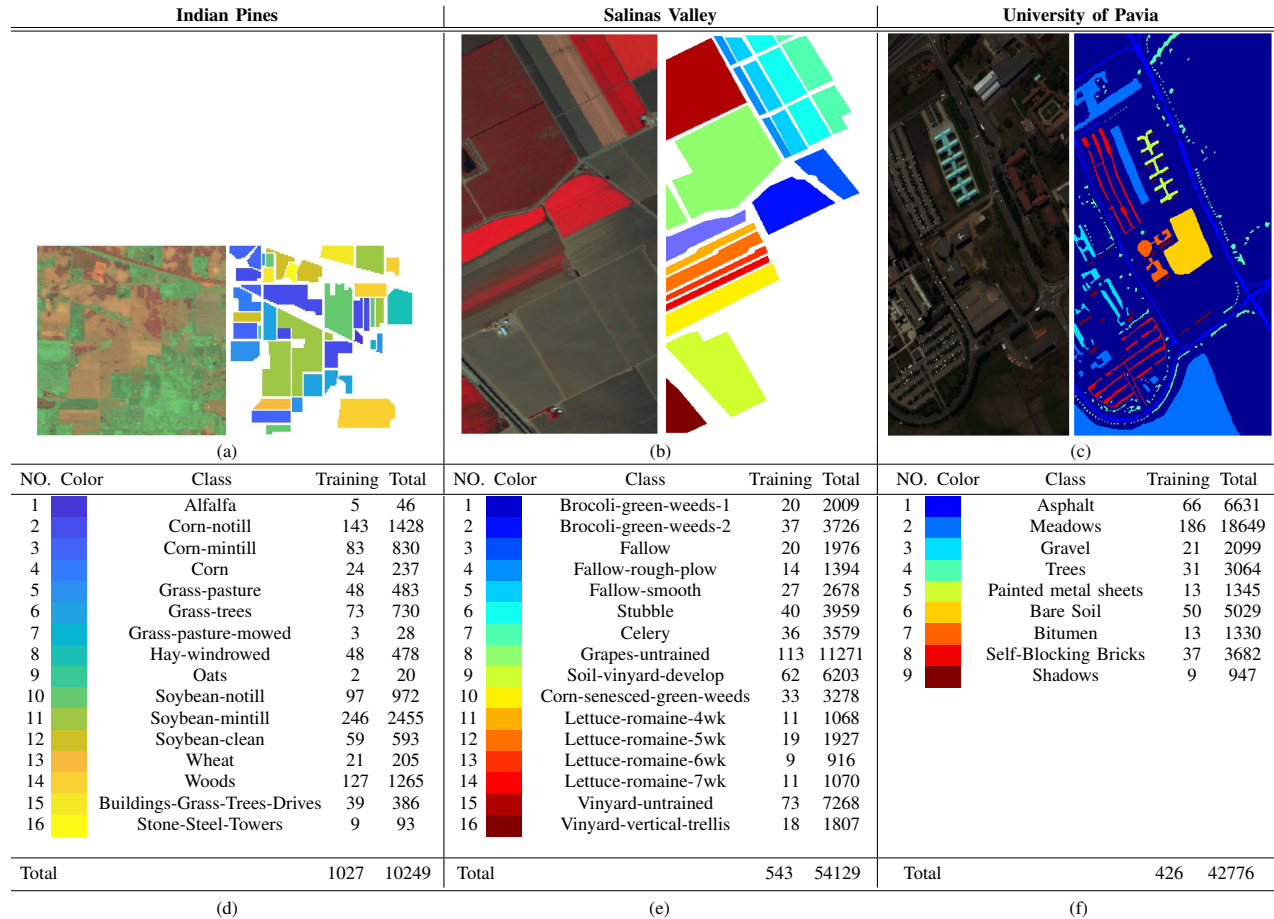


Fig. 7. (Left) False color maps and (Right) ground-truth maps of three HSI data sets. (a) Indian Pines (bands 20, 40, and 60). (b) Salinas Valley (bands 46, 27, and 10). (c) University of Pavia (bands 47, 27, and 13). (d)-(f) show the number of training samples.

TABLE I  
THE PARAMETER SETTINGS OF 2-D CNN AND 3-D CNN

2-D CNN				3-D CNN			
Layer Name	Output Shape	Filter Size	Padding	Layer Name	Output Shape	Filter Size	Padding
Input Layer	27 × 27	N/A	N/A	Input Layer	10 × 27 × 27	N/A	N/A
Convolutional Layer	27 × 27 × 32	4 × 4 × 32	SAME	Convolutional Layer	10 × 27 × 27 × 32	4 × 4 × 4 × 32	SAME
MaxPooling Layer	13 × 13 × 32	2 × 2 × 32	SAME	MaxPooling Layer	5 × 13 × 13 × 32	2 × 2 × 2 × 32	SAME
Convolutional Layer	13 × 13 × 64	5 × 5 × 64	SAME	Convolutional Layer	5 × 13 × 13 × 64	5 × 5 × 5 × 64	SAME
MaxPooling Layer	6 × 6 × 64	2 × 2 × 64	SAME	MaxPooling Layer	3 × 6 × 6 × 64	2 × 2 × 2 × 64	SAME
Dropout	6 × 6 × 64	0.5	N/A	Dropout	3 × 6 × 6 × 64	0.5	N/A
Convolutional Layer	6 × 6 × 128	4 × 4 × 128	SAME	Convolutional Layer	3 × 6 × 6 × 128	4 × 4 × 4 × 128	SAME
Dropout	6 × 6 × 128	0.5	N/A	Dropout	3 × 6 × 6 × 128	0.5	N/A
Flatten	4608	N/A	N/A	Flatten	13824	N/A	N/A
Dense Layer	128	N/A	N/A	Dense Layer	128	N/A	N/A
Output	N	N/A	N/A	Output	N	N/A	N/A

\* N in the above table denotes the number of classes in the HSI data sets.

According to [54], fivefold cross-validation is adopted to tune  $C$  and  $\gamma$  from the range of  $\{2^{-5}, 2^{-4}, \dots, 2^{19}\}$  and  $\{2^{-15}, 2^{-14}, \dots, 2^4\}$ , respectively. For 2-D CNN and 3-D CNN, the parameter settings are summarized in Table I according to [24]. As for SaLSTM, SeLSTM, and SSLSTMs [50], the number of output nodes in SeLSTM and SaLSTM are set as 64 and 128, respectively, for the Indian Pines and Salinas Valley data sets, and they are 128 and 256 for the University of Pavia data set. More importantly, the detailed parameter settings for the proposed SaCL2DNN, SSCL2DNN, and SSCL3DNN

models are summarized in Tables II-IV. In addition, the size of the local window of each pixel in these three data sets is fixed as  $27 \times 27$  according to [24]. In order to make the loss function of the proposed deep models converge to the greatest extent, the number of training epochs is fixed as 2000. The learning rate is fixed as 0.001 from epochs 1 to 2000 for SSCL2DNN while 0.0001 for SaCL2DNN and SSCL3DNN.

TABLE II  
THE PARAMETER SETTINGS OF THE PROPOSED SaCL2DNN  
MODEL

Layer Name	Output Shape	Filter Size	Padding
Input Layer	$27 \times 27$	N/A	N/A
ConvLSTM2D Layer	$27 \times 27 \times 32$	$3 \times 3 \times 32$	SAME
MaxPooling Layer	$14 \times 14 \times 32$	$2 \times 2 \times 32$	SAME
ConvLSTM2D Layer	$14 \times 14 \times 64$	$5 \times 5 \times 64$	SAME
MaxPooling Layer	$7 \times 7 \times 64$	$2 \times 2 \times 64$	SAME
Droup	$7 \times 7 \times 64$	0.25	N/A
Flatten	3136	N/A	N/A
Dense Layer	128	N/A	N/A
Output	N	N	N/A

TABLE III  
THE PARAMETER SETTINGS OF THE PROPOSED SSCL2DNN  
MODEL

Layer Name	Output Shape	Filter Size	Padding
Input Layer	$10 \times 27 \times 27$	N/A	N/A
ConvLSTM2D Layer	$10 \times 27 \times 27 \times 32$	$4 \times 4 \times 32$	SAME
MaxPooling Layer	$10 \times 14 \times 14 \times 32$	$2 \times 2 \times 32$	SAME
ConvLSTM2D Layer	$1 \times 14 \times 14 \times 64$	$3 \times 3 \times 64$	SAME
MaxPooling Layer	$1 \times 7 \times 7 \times 64$	$2 \times 2 \times 64$	SAME
Droup	$1 \times 7 \times 7 \times 64$	0.25	N/A
Flatten	3136	N/A	N/A
Dense Layer	128	N/A	N/A
Output	N	N	N/A

TABLE IV  
THE PARAMETER SETTINGS OF THE PROPOSED SSCL3DNN  
MODEL

Layer Name	Output Shape	Filter Size	Padding
Input Layer	$10 \times 27 \times 27$	N/A	N/A
ConvLSTM3D Layer	$10 \times 27 \times 27 \times 32$	$4 \times 4 \times 4 \times 32$	SAME
MaxPooling Layer	$5 \times 14 \times 14 \times 32$	$2 \times 2 \times 2 \times 32$	SAME
ConvLSTM3D Layer	$5 \times 14 \times 14 \times 64$	$3 \times 3 \times 3 \times 64$	SAME
MaxPooling Layer	$3 \times 7 \times 7 \times 64$	$2 \times 2 \times 2 \times 64$	SAME
Droup	$3 \times 7 \times 7 \times 64$	0.25	N/A
Flatten	9408	N/A	N/A
Dense Layer	128	N/A	N/A
Droup	128	0.5	N/A
Output	N	N	N/A

For hardware system configuration, all the following experiments are completed on a desktop with an 8th Generation Intel Core i7-8700 processor and up to 3.7 GHz, 16 GB of DDR4 RAM with a serial speed of 2400 MHz, a Nvidia GeForce GTX 1080ti GPU with 11 GB memory, an Inter SSD D3-S4510 with 240GB. For software system configuration, we adopt Ubuntu 16.04.4 x64 as our operating system for all experiments. CUDA 8.0 and cuDNN 7.0.5, Tflearn with 0.3.2, Tensorflow-gpu with 1.4.0 and python 3.5.4 are the main programming environment. Specially, all methods involved in our experiments are completed in Anaconda 3.4.

It should be noted that Tflearn is a modular and transparent deep learning library built on Tensorflow, and can provide a higher level API than Tensorflow. A combination of Tflearn and Tensorflow constructs the core framework of the proposed deep models.

### C. Classification Performance

In order to show the superiority of the proposed deep models, we randomly select 1% of the available labeled samples for training for both the Salinas Valley and University of Pavia data while 10% for the Indian

Pines data, respectively. And the remaining samples are used for testing. For SVM, 2-D CNN, SaLSTM, and SaCL2DNN, the number of components after conducting PCA on the original data is set as 1. As for 3-D CNN, SSLSTMs, SSCL2DNN and SSCL3DNN, 10 components are preserved.

According to the experiment settings in Subsection B, the quantitative assessments based on all models are reported in Tables V-VII, from which it can be seen that the proposed SaCL2DNN, SSCL2DNN and SSCL3DNN models can provide better classification performance than other considered models. First of all, three special gate mechanisms make it possible for ConvLSTM to take full use of both the spatial and spectral information of HSIs than CNN that operated by the traditional method based on the sliding window. What's more, the implementations of the gate mechanisms in ConvLSTM are extended from one-dimensional to multi-dimensional convolution operation, which enables ConvLSTM to better preserve and capture the spatial context information of HSIs, and fuse the spatial and spectral information more effectively than LSTM. Specifically, on the one hand, Compared with 2-D CNN, the proposed SaCL2DNN model improves OA, AA, and  $\kappa$  by 0.86%, 0.37%, and 0.99%, respectively, when considering the Indian Pines data set. As for the Salinas Valley data set, the improvements of OA, AA, and  $\kappa$  are 5.03%, 5.13%, and 5.59%, respectively. And for the University of Pavia data set, the gains of OA, AA, and  $\kappa$  are 4.80%, 4.42%, and 6.08%, respectively. It should be pointed out that it is the loss of the spatial information that leads to unsatisfactory classification results for SVM and SaLSTM. As shown in Fig. 4, SaCL2DNN is a special case of SSCL2DNN. For SSCL2DNN, it shows better performance than SaCL2DNN, and obtains 0.65%, 1.62%, and 3.37% gains in OA for these three HSI data sets, respectively. The experimental results shown in Tables V-VII verify the effectiveness of the proposed SSCL2DNN model, and demonstrate that joint learning of spectral and spatial features by modeling long-range dependencies in the spectral dimension can provide higher classification performance than SaCL2DNN.

On the other hand, as shown in Tables V-VII, the proposed SSCL3DNN model fuses spatial and spectral information more effectively to further improve the classification accuracy and yields the best classification result among all spatial-spectral models considered in this paper. Compared with 3-D CNN, the improvement in OA provided by SSCL3DNN are 0.51%, 2.12%, and 7.96% for three data sets, respectively. In particular, the proposed SSCL3DNN model produces the remarkable gains in OA, AA, and  $\kappa$  for the Salinas Valley and University of Pavia data sets. From Tables V-VII, it can be seen that the 3-D extended architecture (ConvLSTM3D) of LSTM makes it possible for the proposed SSCL3DNN

TABLE V  
CLASSIFICATION RESULTS FOR THE INDIAN PINES DATA SET USING 10% TRAINING SAMPLES

Class	SVM	2-D CNN	SaLSTM	SaCL2DNN	3-D CNN	SSLSTMs	SSCL2DNN	SSCL3DNN
1	70.73	<b>90.24</b>	85.98	86.59	<b>99.39</b>	79.88	92.68	98.17
2	89.32	95.47	92.43	<b>96.73</b>	97.86	94.24	97.78	<b>99.12</b>
3	91.93	<b>95.21</b>	87.25	94.31	<b>97.05</b>	90.70	95.65	96.52
4	86.50	92.84	88.97	<b>93.54</b>	96.95	88.85	96.13	<b>98.71</b>
5	90.57	<b>94.02</b>	91.49	91.55	96.55	91.09	95.86	<b>97.07</b>
6	97.72	97.45	95.81	<b>98.36</b>	<b>99.20</b>	96.58	98.82	99.09
7	58.00	<b>75.00</b>	67.00	74.00	94.00	77.00	93.00	<b>96.00</b>
8	98.72	99.07	96.16	<b>99.71</b>	<b>100.00</b>	97.09	99.53	<b>100.00</b>
9	44.44	61.11	59.72	<b>63.89</b>	<b>76.39</b>	63.89	62.50	63.89
10	77.20	94.86	89.37	<b>95.54</b>	97.31	91.49	97.09	<b>98.74</b>
11	95.02	98.03	95.30	<b>99.33</b>	98.95	95.21	98.71	<b>99.33</b>
12	84.27	91.06	85.53	<b>95.27</b>	97.94	86.42	96.40	<b>98.78</b>
13	89.13	93.75	86.68	<b>97.96</b>	97.01	91.98	95.24	<b>99.73</b>
14	97.41	98.79	97.72	<b>99.34</b>	99.56	98.51	99.65	<b>99.69</b>
15	93.73	97.33	95.24	<b>98.70</b>	99.06	94.42	98.20	<b>99.42</b>
16	68.75	<b>93.15</b>	70.83	88.39	<b>94.35</b>	79.46	88.99	92.56
OA	91.20	96.21	92.59	<b>97.07</b>	98.28	93.69	97.72	<b>98.79</b>
AA	83.34	91.71	86.59	<b>92.08</b>	<b>96.35</b>	88.56	94.14	96.05
$\kappa$	89.91	95.67	91.53	<b>96.66</b>	98.04	92.79	97.40	<b>98.62</b>

TABLE VI  
CLASSIFICATION RESULTS FOR THE SALINAS VALLEY DATA SET USING 1% TRAINING SAMPLES

Class	SVM	2-D CNN	SaLSTM	SaCL2DNN	3-D CNN	SSLSTMs	SSCL2DNN	SSCL3DNN
1	74.26	81.35	89.66	<b>96.68</b>	98.59	82.02	91.64	<b>99.73</b>
2	85.23	86.21	76.85	<b>97.40</b>	99.96	82.15	97.80	<b>100.00</b>
3	59.56	78.14	51.94	<b>81.61</b>	96.22	54.62	98.77	<b>100.00</b>
4	98.19	97.66	95.97	<b>99.13</b>	99.81	95.53	99.40	<b>100.00</b>
5	94.33	93.45	93.66	<b>97.62</b>	<b>99.66</b>	93.05	98.83	99.14
6	94.40	94.61	94.01	<b>99.63</b>	99.98	95.74	100.00	<b>100.00</b>
7	78.97	88.90	80.20	<b>95.48</b>	98.74	82.30	96.23	<b>100.00</b>
8	85.36	93.66	82.68	<b>93.52</b>	89.17	85.36	93.05	<b>97.36</b>
9	68.44	84.14	80.87	<b>95.91</b>	99.84	77.75	99.89	<b>99.97</b>
10	71.65	87.81	70.49	<b>95.78</b>	99.04	70.77	98.44	<b>99.76</b>
11	93.98	94.54	97.67	<b>96.53</b>	97.45	95.90	98.08	<b>99.68</b>
12	88.38	87.47	84.22	<b>95.25</b>	99.09	86.60	99.06	<b>100.00</b>
13	80.04	82.21	72.14	<b>86.99</b>	97.46	68.72	97.02	<b>99.45</b>
14	84.04	88.10	92.73	<b>93.08</b>	<b>99.84</b>	91.34	99.69	99.75
15	90.36	94.59	86.30	<b>98.11</b>	<b>99.49</b>	88.93	92.78	99.48
16	64.92	<b>78.96</b>	64.82	71.16	99.85	61.13	93.39	<b>100.00</b>
OA	82.39	89.65	82.28	<b>94.68</b>	97.17	83.10	96.30	<b>99.29</b>
AA	82.01	88.24	82.14	<b>93.37</b>	98.39	81.99	97.13	<b>99.65</b>
$\kappa$	80.30	88.47	80.26	<b>94.06</b>	96.85	81.15	95.88	<b>99.21</b>

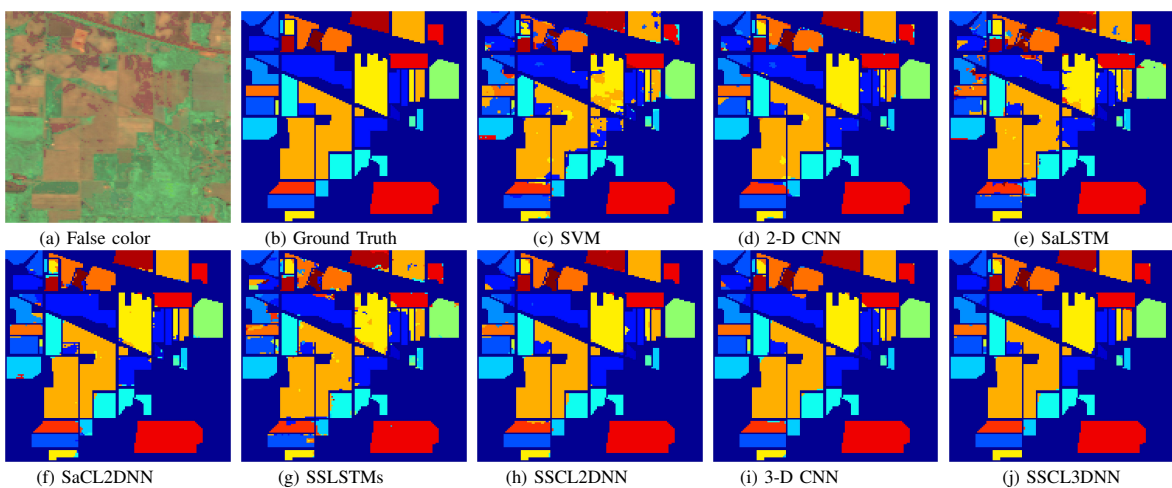


Fig. 8. Classification maps for the Indian Pines data set. (a) False color map. (b) Ground-truth map. (c) SVM. (d) 2-D CNN. (e) SaLSTM. (f) SaCL2DNN. (g) SSLSTMs. (h) SSCL2DNN. (i) 3-D CNN. (j) SSCL3DNN.

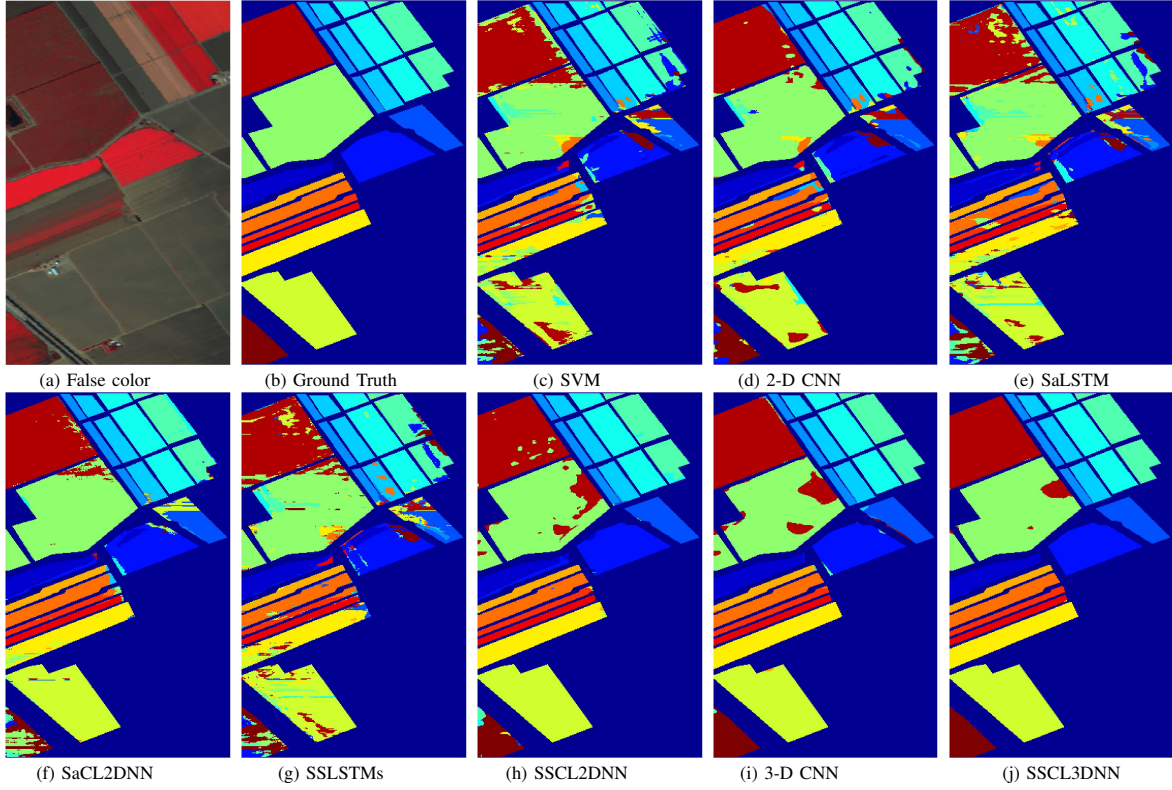


Fig. 9. Classification maps for the Salinas Valley data set. (a) False color map. (b) Ground-truth map. (c) SVM. (d) 2-D CNN. (e) SaLSTM. (f) SaCL2DNN. (g) SSLSTMs. (h) SSCL2DNN. (i) 3-D CNN. (j) SSCL3DNN.

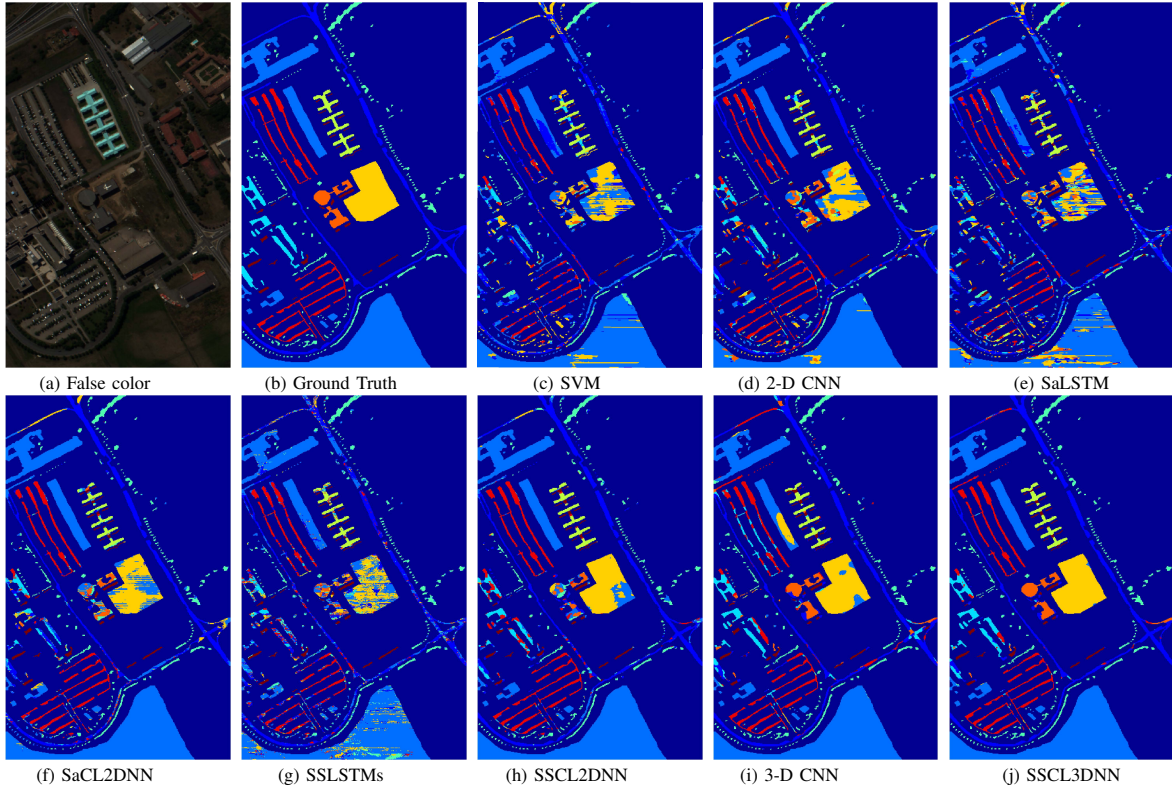


Fig. 10. Classification maps for the University of Pavia data set. (a) False color map. (b) Ground-truth map. (c) SVM. (d) 2-D CNN. (e) SaLSTM. (f) SaCL2DNN. (g) SSLSTMs. (h) SSCL2DNN. (i) 3-D CNN. (j) SSCL3DNN.

TABLE VII  
CLASSIFICATION RESULTS FOR THE UNIVERSITY OF PAVIA DATA SET USING 1% TRAINING SAMPLES

Class	SVM	2-D CNN	SaLSTM	SaCL2DNN	3-D CNN	SSLSTMs	SSCL2DNN	SSCL3DNN
1	52.21	79.64	57.22	<b>80.20</b>	82.91	70.57	90.32	<b>97.62</b>
2	89.78	93.79	81.84	<b>98.54</b>	96.25	89.90	98.72	<b>99.95</b>
3	17.73	44.26	27.74	<b>45.76</b>	66.25	32.20	55.37	<b>82.96</b>
4	55.23	77.30	57.98	<b>81.89</b>	90.61	69.21	78.87	<b>96.52</b>
5	68.05	77.76	70.80	<b>79.55</b>	93.83	77.69	87.42	<b>98.51</b>
6	39.14	70.75	42.07	<b>85.55</b>	85.72	50.47	87.04	<b>97.75</b>
7	15.19	<b>38.22</b>	27.46	36.05	77.80	35.20	35.91	<b>88.61</b>
8	60.56	84.19	62.86	<b>87.23</b>	88.48	68.19	91.34	<b>95.41</b>
9	53.39	79.13	57.23	<b>90.06</b>	68.64	85.37	75.59	<b>83.60</b>
OA	65.67	81.89	64.77	<b>86.69</b>	89.14	73.90	89.04	<b>97.10</b>
AA	50.14	71.67	53.91	<b>76.09</b>	83.39	64.31	77.84	<b>93.44</b>
$\kappa$	51.52	75.86	52.90	<b>81.94</b>	85.59	64.42	85.16	<b>96.14</b>

model to handle the multidimensional data, and the gate mechanisms in ConvLSTM3D enable SSCL3DNN to extract more discriminative spatial-spectral features for HSI classification.

Corresponding to Tables V-VII, similar conclusions can be drawn from the classification maps presented in Figs. 8-10, from which it is obvious that the proposed SSCL3DNN model can provide the best classification maps, which are closest to the ground-truth maps for these three HSI data sets. In addition, there are only fewer misclassifications, and the clear boundaries of each class in the classification maps are better recognized.

As we all know, it is greatly expensive and difficult to obtain samples with labels. Therefore, it is necessary to investigate the performance under small training size.

#### D. Sensitivity Comparison and Analysis under Small Samples

In order to further demonstrate the performance of the proposed deep models, we randomly select 10 samples from each available labeled class to construct smaller training sets.

The experimental results are reported in Tables VIII-IX, from which it can be observed that even in the case of small size of training samples, the proposed deep models can also show better classification performance. In particular, the proposed SaCL2DNN model can better capture spatial context information of the original data, and obtain satisfactory performance even in the case of small training samples. As shown in Tables VIII-IX, compared with 2-D CNN, the improvements in OA yielded by SaCL2DNN are 4.39%, 5.34%, and 16.46%, respectively. SSCL2DNN further improves the classification performance of SaCL2DNN and obtains 3.61%, 15.43%, and 4.44% gains in OA, respectively. In particular, the proposed SSCL3DNN model generates the best classification performance, and the gains in OA are 2.07%, 4.96%, and 22.61%, respectively, when compared with 3-D CNN. More detailed classification results are reported in Tables VIII-IX, which further demonstrate the advantages of the proposed deep models.

To further show the effectiveness of the proposed deep models, 20, 30, and 40 samples from each class are

randomly extracted for training in these three HSI data sets. In particular, the number of training sample for class 7 and class 9 in the Indian Pines data set is fixed as 10. When taking different numbers of training samples into account, the OA curves of all models are provided in Fig. 11, from which it can be seen that for all the three HSI data sets, the proposed SSCL3DNN model provides the highest classification accuracy. It is worth noting that the proposed deep models obtain significant performance improvements in the Salinas Valley and University of Pavia data sets, which also demonstrates the superiority of the proposed deep methods. The experimental results shown in Tables VII-IX and Fig. 11 further demonstrate that the proposed deep models based on ConvLSTM are more effective, and the design of gate mechanisms in ConvLSTM makes it possible for the proposed deep models to extract more effective and discriminative features.

## VI. CONCLUSION

In this paper, two novel deep network models constructed with ConvLSTM have been proposed to extract more effective and discriminative spatial-spectral features for HSI classification. By taking the local data patch as a sequence and feeding in each memory cell band by band, SSCL2DNN was proposed for modeling long-range dependencies in the spectral domain to fuse the spatial and spectral information of HSIs, which is more effective than other approaches that utilize independent channels to extract spatial-spectral features. In particular, a new deep model (SaCL2DNN) derived from SSCL2DNN can take full use of spatial context information of HSIs to obtain a more effective spatial feature representation than CNN, which can be used as an effective spatial feature extraction model for object detection, object location, or others applications. Furthermore, in order to further improve classification performance, the 3-D extended architecture of LSTM (ConvLSTM3D) was constructed, followed by a new SSCL3DNN model to provide more discriminative spatial-spectral features. The experimental results conducted on three widely used HSI data sets show that the proposed deep models offer

TABLE VIII  
CLASSIFICATION RESULTS OF TRAINING UNDER SMALL SAMPLES (10 SAMPLES FOR EACH CLASS)

Class	Indian Pines				Salinas Valley				University of Pavia			
	SVM	2-D CNN	SaLSTM	SaCL2DNN	SVM	2-D CNN	SaLSTM	SaCL2DNN	SVM	2-D CNN	SaLSTM	SaCL2DNN
1	91.67	94.44	88.33	<b>95.00</b>	73.31	76.16	70.96	<b>83.71</b>	40.07	37.14	32.95	<b>44.89</b>
2	<b>42.99</b>	37.83	31.20	38.98	58.15	61.93	47.37	<b>73.62</b>	42.49	43.51	30.42	<b>67.08</b>
3	<b>56.51</b>	47.59	41.90	52.34	53.38	46.20	36.31	<b>67.70</b>	30.80	<b>34.96</b>	21.97	34.67
4	73.83	76.12	65.37	<b>84.93</b>	95.94	97.34	93.05	<b>99.21</b>	54.21	59.74	31.83	<b>66.72</b>
5	56.87	58.01	57.67	<b>63.00</b>	87.47	88.78	82.36	<b>92.50</b>	<b>83.97</b>	75.18	69.46	80.02
6	<b>60.42</b>	46.06	43.86	51.44	<b>87.51</b>	85.21	81.16	82.60	33.57	23.30	18.84	<b>45.57</b>
7	97.78	<b>100.00</b>	94.44	<b>100.00</b>	63.57	68.06	60.57	<b>82.64</b>	<b>66.39</b>	35.86	33.23	39.77
8	<b>96.28</b>	93.33	70.56	87.78	37.40	<b>38.37</b>	40.94	32.38	43.75	63.47	30.15	<b>79.58</b>
9	<b>100.00</b>	<b>100.00</b>	84.00	<b>100.00</b>	43.82	34.70	40.19	<b>45.79</b>	57.42	86.27	57.45	<b>95.55</b>
10	52.77	47.80	42.64	<b>56.30</b>	53.64	53.20	47.65	<b>83.46</b>				
11	<b>42.94</b>	42.45	28.09	42.81	94.67	93.01	89.21	<b>96.07</b>				
12	49.67	45.97	38.42	<b>52.08</b>	89.17	80.86	69.13	<b>90.28</b>				
13	81.13	86.97	75.18	<b>95.90</b>	90.53	93.09	85.76	<b>94.88</b>				
14	70.66	69.94	73.34	<b>82.10</b>	90.60	87.72	88.72	<b>97.96</b>				
15	71.33	69.95	67.98	<b>78.67</b>	<b>81.05</b>	78.31	77.32	72.90				
16	90.84	90.60	77.11	<b>92.77</b>	73.32	61.37	51.50	<b>82.53</b>				
OA	56.41	53.08	45.77	<b>57.47</b>	63.77	62.15	59.15	<b>67.49</b>	43.81	44.30	31.02	<b>60.76</b>
AA	70.98	69.19	61.26	<b>73.38</b>	73.28	71.52	66.39	<b>79.89</b>	50.30	51.05	36.26	<b>61.54</b>
$\kappa$	51.34	47.72	40.40	<b>52.75</b>	60.24	58.56	55.22	<b>64.47</b>	32.36	32.59	19.04	<b>50.60</b>

TABLE IX  
CLASSIFICATION RESULTS OF TRAINING UNDER SMALL SAMPLES (10 SAMPLES FOR EACH CLASS)

Class	Indian Pines				Salinas Valley				University of Pavia			
	3-D CNN	SSLSTMs	SSCL2DNN	SSCL3DNN	3-D CNN	SSLSTMs	SSCL2DNN	SSCL3DNN	3-D CNN	SSLSTMs	SSCL2DNN	SSCL3DNN
1	97.22	86.11	100.00	<b>100.00</b>	<b>99.84</b>	74.81	79.13	99.69	42.58	39.94	49.94	<b>69.89</b>
2	<b>53.60</b>	35.35	44.80	53.30	89.36	50.32	70.94	<b>99.90</b>	<b>84.89</b>	29.08	76.94	82.44
3	<b>61.78</b>	38.44	51.07	50.37	92.56	39.67	98.80	<b>99.93</b>	25.50	25.10	44.77	<b>65.10</b>
4	<b>96.83</b>	62.03	78.50	88.63	99.36	94.86	98.22	<b>99.83</b>	34.01	60.82	55.16	<b>90.48</b>
5	75.90	61.27	65.33	<b>76.58</b>	96.25	83.22	94.80	<b>98.01</b>	91.41	73.71	90.51	<b>94.83</b>
6	78.47	40.39	70.69	<b>90.17</b>	99.22	90.47	94.02	<b>99.67</b>	37.47	29.14	41.64	<b>82.37</b>
7	<b>100.00</b>	97.78	100.00	<b>100.00</b>	95.39	66.74	87.12	<b>99.74</b>	80.61	40.66	58.66	<b>89.32</b>
8	99.83	71.67	99.83	<b>100.00</b>	<b>87.12</b>	44.20	65.67	85.00	10.74	34.70	71.68	<b>84.71</b>
9	<b>100.00</b>	92.00	96.00	<b>100.00</b>	96.33	40.61	97.44	<b>99.73</b>	21.10	85.91	91.89	<b>86.91</b>
10	63.56	44.86	62.25	<b>75.36</b>	95.18	47.55	91.98	<b>99.04</b>				
11	55.09	32.74	49.30	<b>59.66</b>	97.05	89.62	98.03	<b>99.41</b>				
12	<b>67.03</b>	42.98	51.15	64.97	97.27	71.95	97.00	<b>99.69</b>				
13	96.82	82.87	96.82	<b>99.79</b>	98.87	85.52	98.92	<b>99.65</b>				
14	88.11	71.81	70.98	<b>88.29</b>	98.49	87.13	97.00	<b>99.75</b>				
15	84.20	66.60	84.89	<b>87.66</b>	63.49	77.58	71.52	<b>86.22</b>				
16	98.31	86.99	96.39	<b>100.00</b>	95.72	51.60	79.59	<b>99.98</b>				
OA	69.21	47.57	61.08	<b>71.28</b>	89.77	61.63	82.92	<b>94.73</b>	58.50	36.33	65.20	<b>81.11</b>
AA	82.30	63.37	76.12	<b>83.42</b>	93.84	68.49	88.76	<b>97.83</b>	47.59	46.56	64.58	<b>82.90</b>
$\kappa$	65.56	42.16	56.58	<b>67.83</b>	88.57	57.92	81.05	<b>94.14</b>	44.68	25.33	55.45	<b>75.65</b>

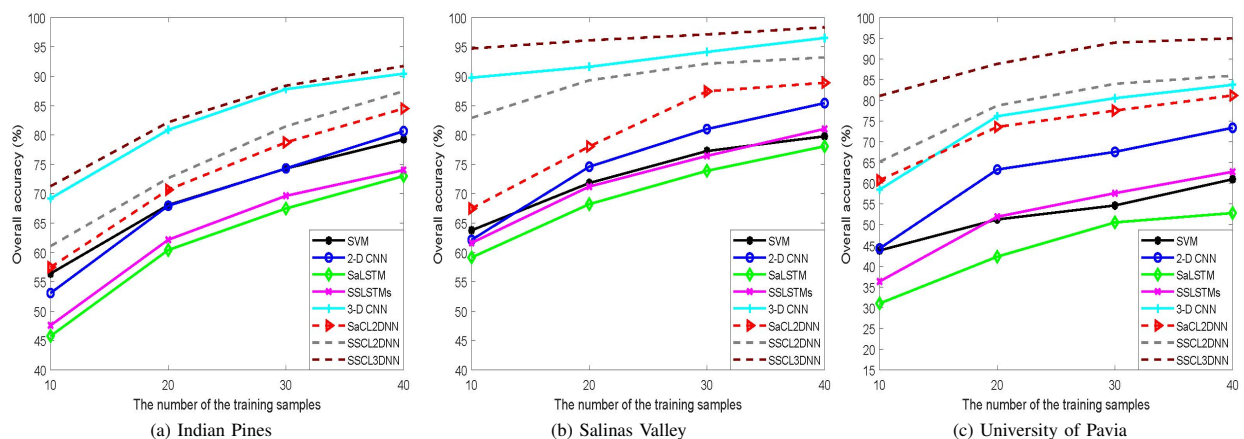


Fig. 11. Overall accuracy (%) of considered methods with different number of training samples for three HSI data sets: (a) Indian Pines, (b) Salinas Valley, (c) University of Pavia.

competitive advantages over state-of-the-art approaches, especially in the case of small training size.

## REFERENCES

- [1] D. Landgrebe, "Hyperspectral image data analysis," *IEEE Signal Process. Mag.*, vol. 19, no. 1, pp. 17-28, Jan. 2002.
- [2] J. M. Bioucas-Dias, A. Plaza, G. Camps-Valls, P. Scheunders, N. Nasrabadi, and J. Chanussot, "Hyperspectral remote sensing data analysis and future challenges," *IEEE Geosci. Remote Sens. Mag.*, vol. 1, no. 2, pp. 6-36, Jun. 2013.
- [3] G. Camps-Valls, D. Tuia, L. Bruzzone, and J. A. Benediktsson, "Advances in hyperspectral image classification: Earth monitoring with statistical learning methods," *IEEE Signal Process. Mag.*, vol. 31, no. 1, pp. 45-54, Jan. 2014.
- [4] X. Zhang, Y. Sun, K. Shang, L. Zhang, and S. Wang, "Crop classification based on feature band set construction and object-oriented approach using hyperspectral images," *IEEE J. Sel. Topics Appl. Earth Observ. Remote Sens.*, vol. 9, no. 9, pp. 4117-4128, Sep. 2016.
- [5] F. M. Lacar, M. M. Lewis, and I. T. Grierson, "Use of hyperspectral imagery for mapping grape varieties in the Barossa Valley, South Australia," in *IEEE Int. Geosci. Remote Sens. Symp.*, Sydney, NSW, Australia, Jul. 2001, pp. 2875-2877.
- [6] A. Ghiyamat and H. Z. Shafri, "A review on hyperspectral remote sensing for homogeneous and heterogeneous forest biodiversity assessment," *Int. J. Remote Sens.*, vol. 31, no. 7, pp. 1837-1856, 2010.
- [7] F. van der Meer, "Analysis of spectral absorption features in hyperspectral imagery," *Int. J. Appl. Earth Observ. Geoinf.*, vol. 5, no. 1, pp. 55-68, Feb. 2004.
- [8] F. Melgani and L. Bruzzone, "Classification of hyperspectral remote sensing images with support vector machines," *IEEE Trans. Geosci. Remote Sens.*, vol. 42, no. 8, pp. 1778-1790, Aug. 2004.
- [9] L. Pan, H. Li, W. Li, X. Chen, G. Wu, and Q. Du, "Discriminant analysis of hyperspectral imagery using fast kernel sparse and low-rank graph," *IEEE Trans. Geosci. Remote Sens.*, vol. 55, no. 11, pp. 6085-6098, Nov. 2017.
- [10] G. Camps-Valls, L. Gomez-Chova, J. Munoz-Mari, J. Vilafrances, and J. Calpe-Maravilla, "Composite kernels for hyperspectral image classification," *IEEE Geosci. Remote Sens. Lett.*, vol. 3, no. 1, pp. 93-97, Jan. 2006.
- [11] J. Wright, A. Y. Yang, A. Ganesh, S. S. Sastry, and Y. Ma, "Robust face recognition via sparse representation," *IEEE Trans. Pattern Anal. Mach. Intell.*, vol. 31, no. 2, pp. 210-227, Feb. 2009.
- [12] M. Cui and S. Prasad, "Class-dependent sparse representation classifier for robust hyperspectral image classification," *IEEE Trans. Geosci. Remote Sens.*, vol. 53, no. 5, pp. 2683-2695, May 2015.
- [13] Y. Chen, N. M. Nasrabadi, and T. D. Tran, "Hyperspectral image classification using dictionary-based sparse representation," *Remote Sens.*, vol. 49, no. 10, pp. 3973-3985, Oct. 2011.
- [14] H. Zhang, J. Li, Y. Huang, and L. Zhang, "A nonlocal weighted joint sparse representation classification method for hyperspectral imagery," *IEEE J. Sel. Topics Appl. Earth Observ. Remote Sens.*, vol. 7, no. 6, pp. 2056-2065, Jun. 2014.
- [15] C. Chen, N. Chen, and J. Peng, "Nearest regularized joint sparse representation for hyperspectral image classification," *IEEE Geosci. Remote Sens. Lett.*, vol. 13, no. 3, pp. 424-428, Mar. 2016.
- [16] J. Peng and Q. Du, "Robust joint sparse representation based on maximum correntropy criterion for hyperspectral image classification," in *IEEE Trans. Geosci. Remote Sens.*, vol. 55, no. 12, pp. 7152-7164, Dec. 2017.
- [17] S. Ren, K. He, R. Girshick, and J. Sun, "Faster R-CNN: Towards real-time object detection with region proposal networks," *IEEE Trans. Pattern Anal. Mach. Intell.*, vol. 39, no. 6, pp. 1137-1149, Jun. 2017.
- [18] G. Zhu, F. Porikli, and H. Li, "Robust visual tracking with deep convolutional neural network based object proposals on pets," in *IEEE Conf. Comput. Vis. Pattern Recognit. Workshops*, Las Vegas, NV, 2016, pp. 1265-1272.
- [19] A. N. Shuaibu, A. S. Malik, and I. Faye, "Adaptive feature learning CNN for behavior recognition in crowd scene," in *IEEE Int. Conf. Signal Image Process. Appl.*, Kuching, 2017, pp. 357-361.
- [20] F. Ratle, G. Camps-Valls, and J. Weston, "Semisupervised neural networks for efficient hyperspectral image classification," *IEEE Trans. Geosci. Remote Sens.*, vol. 48, no. 5, pp. 2271-2282, May 2010.
- [21] T. Li, J. Zhang, and Y. Zhang, "Classification of hyperspectral image based on deep belief networks," in *Proc. IEEE Int. Conf. Image Process.*, Paris, France, 2014, pp. 5132-5136.
- [22] W. Hu, Y. Huang, W. Li, F. Zhang, and H. Li, "Deep Convolutional Neural Networks for Hyperspectral Image Classification," *Journal of Sensors*, vol. 2015, no. 2, pp. 1-12, Jul. 2015.
- [23] Y. Chen, Z. Lin, X. Zhao, G. Wang, and Y. Gu, "Deep learning-based classification of hyperspectral data," *IEEE J. Sel. Topics Appl. Earth Observ. Remote Sens.*, vol. 7, no. 6, pp. 2094-2107, Jun. 2014.
- [24] Y. Chen, H. Jiang, C. Li, X. Jia, and P. Ghamisi, "Deep feature extraction and classification of hyperspectral images based on convolutional neural networks," *IEEE Trans. Geosci. Remote Sens.*, vol. 54, no. 10, pp. 6232-6251, Oct. 2016.
- [25] S. Mei, J. Ji, Q. Bi, J. Hou, Q. Du, and W. Li, "Integrating spectral and spatial information into deep convolutional neural networks for hyperspectral classification," in *Proc. Int. Geosci. Remote Sens. Symp.*, Beijing, 2016, pp. 5067-5070.
- [26] W. Li, G. Wu, F. Zhang, and Q. Du, "Hyperspectral image classification using deep pixel-pair features," *IEEE Trans. Geosci. Remote Sens.*, vol. 55, no. 2, pp. 844-853, Feb. 2017.
- [27] W. Shao and S. Du, "Spectral-spatial feature extraction for hyperspectral image classification: A dimension reduction and deep learning approach," *IEEE Trans. Geosci. Remote Sens.*, vol. 54, no. 8, pp. 4544-4554, Oct. 2016.
- [28] Z. Zhong, J. Li, Z. Luo, and M. Chapman, "Spectral-spatial residual network for hyperspectral image classification: A 3-D deep learning framework," *IEEE Trans. Geosci. Remote Sens.*, vol. 56, no. 2, pp. 847-858, Feb. 2018.
- [29] Y. Li, H. Zhang, and Q. Shen, "Spectral-spatial classification of hyperspectral imagery with 3D convolutional neural network," *Remote Sens.*, vol. 9, no. 1, pp. 67, Jan. 2017.
- [30] M. E. Paoletti, J. M. Haut, J. Plaza, and A. Plaza, "A new deep convolutional neural network for fast hyperspectral image classification," *ISPRS J. Photogramm. Remote Sens.*, vol. 145, pp. 120-147, Nov. 2018.
- [31] R. Kemker and C. Kanan, "Self-taught feature learning for hyperspectral image classification," *IEEE Trans. Geosci. Remote Sens.*, vol. 55, no. 5, pp. 2693-2705, May 2017.
- [32] B. Liu, X. Yu, P. Zhang, X. Tan, A. Yu, and Z. Xue, "A semi-supervised convolutional neural network for hyperspectral image classification," *Remote Sens. Lett.*, vol. 8, no. 9, pp. 839-848, Sep. 2017.
- [33] B. Liu, X. Yu, P. Zhang, A. Yu, Q. Fu, and X. Wei, "Supervised deep feature extraction for hyperspectral image classification," *IEEE Trans. Geosci. Remote Sens.*, vol. 56, no. 4, pp. 1909-1921, Apr. 2018.
- [34] H. Zhang, Y. Li, Y. Zhang, and Q. Shen, "Spectral-spatial classification of hyperspectral imagery using a dual-channel convolutional neural network," *Remote Sens. Lett.*, vol. 8, no. 5, pp. 438-447, 2017.
- [35] R. K. Srivastava, K. Greff, and J. Schmidhuber, "Training very deep networks," in *Proc. Adv. Neural Inf. Process. Syst.*, 2015, pp. 2377-2385.
- [36] Z. Zhong, J. Li, Z. Luo, and M. Chapman, "Spectral-spatial residual network for hyperspectral image classification: A 3-D deep learning framework," *IEEE Trans. Geosci. Remote Sens.*, vol. 56, no. 2, pp. 847-858, Feb. 2018.
- [37] S. Sabour, N. Frosst, and G. E. Hinton, "Dynamic routing between capsules," in *Proc. Adv. Neural Inf. Process. Syst.*, pp. 3859-3869, 2017.
- [38] M. E. Paoletti, J. M. Haut, J. Plaza, and A. Plaza, "Deep & dense convolutional neural network for hyperspectral image classification," *Remote Sens.*, vol. 10, no. 9, pp. 1454, Sep. 2018.

- [39] A. Graves, M. Liwicki, S. Fernndez, R. Bertolami, H. Bunke, and J. Schmidhuber, "A novel connectionist system for unconstrained handwriting recognition," *IEEE Trans. Pattern Anal. Mach. Intell.*, vol. 31, no. 5, pp. 855-868, May 2009.
- [40] S. Hochreiter and J. Schmidhuber, "Long short-term memory," *Neural comput.*, vol. 9, no. 8, pp. 1735-1780, 1997.
- [41] R. Pascanu, T. Mikolov, and Y. Bengio, "On the difficulty of training recurrent neural networks," in *Proc. 30th Int. Conf. Mach. Learn.*, 2013, pp. 1310-1318.
- [42] I. Sutskever, O. Vinyals, and Q. V. Le, "Sequence to sequence learning with neural networks," in *Proc. Adv. Neural Inf. Process. Syst.*, Montreal, Canada, 2014, pp. 3104-3112.
- [43] Z. C. Lipton, J. Berkowitz, and C. Elkan, "A critical review of recurrent neural network for sequence learning," *Computer Science*, 2015.
- [44] M. Wang, C. Luo, R. Hong, J. Tang, and J. Feng, "Beyond object proposals: Random crop pooling for multi-label image recognition," *IEEE Trans. Image Process.*, vol. 25, no. 12, pp. 5678-5688, Dec. 2016.
- [45] D. Guo, W. Zhou, H. Li, and M. Wang, "Hierarchical lstm for sign language translation," in *Proc. AAAI Conf. Artif. Intell.*, 2018.
- [46] D. Tran, L. Bourdev, R. Fergus, L. Torresani, and M. Paluri, "Learning spatiotemporal features with 3d convolutional networks," in *IEEE Int. Conf. Comput. Vis.*, Santiago, 2015, pp. 4489-4497.
- [47] Z. Yu, G. Liu, Q. Liu, and J. Deng, "Spatio-temporal convolutional features with nested LSTM for facial expression recognition," *Neurocomputing*, vol. 317, pp. 50-57, Nov. 2018.
- [48] Kumar B A et al., "Script identification in natural scene image and video frames using an attention based convolutional-LSTM network," *Pattern Recognit.*, vol. 85, pp. 172-184, Jan. 2019.
- [49] Y. Yang et al., "Video captioning by adversarial LSTM," *IEEE Trans. Image Process.*, vol. 27, no. 11, pp. 5600-5611, Nov. 2018.
- [50] F. Zhou, R. Hang, Q. Liu, and X. Yuan, "Hyperspectral image classification using spectral-spatial LSTMs," *Neurocomputing*, vol. 328, no. 7, pp. 39-47, Feb. 2017.
- [51] X. Shi, Z. Chen, H. Wang, D.-Y. Yeung, W.-k. Wong, and W.-c. Woo, "Convolutional LSTM network: a machine learning approach for precipitation nowcasting," in *Proc. IEEE Conf. Comput. Vis. Pattern Recognit.*, 2015.
- [52] Q. Liu, F. Zhou, R. Hang, and X. Yuan, "Bidirectional convolutional LSTM based spectral-spatial feature learning for hyperspectral image classification," *Remote Sens.*, vol. 9, no. 12, pp. 17-28, Dec. 2017.
- [53] H. Wu and S. Prasad, "Convolutional recurrent neural networks for hyperspectral data classification," *Remote Sens.*, vol. 9, no. 3, pp. 298, Mar. 2017.
- [54] C. Chang and C. Lin, "LIBSVM: A library for support vector machines," *ACM Trans. Intell. Syst. Technol.*, vol. 2, no. 3, pp. 1-27, Mar. 2011.